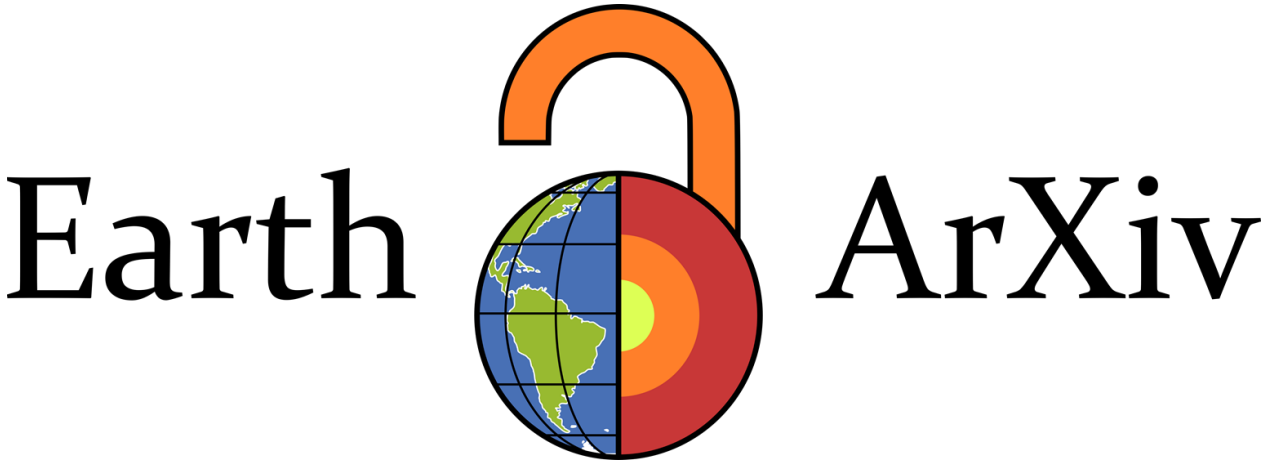

A Phanerozoic Atlas of Earth's Atmosphere, Surface, and Interior Derived from the PANALESIS Plate Tectonic Model

*Florian Franziskakis[1], Niklas Werner[*2], Christian Vérard[3], Sébastien Castelltort[3], Grégory Giuliani[1]*

[1] Institute for Environmental Sciences, University of Geneva
[2] Department of Earth and Planetary Sciences, ETH Zürich
[3] Department of Earth Sciences, University of Geneva

** Corresponding author: Niklas.werner@eaps.ethz.ch*

This manuscript has been submitted for publication in **Nature Scientific Data.** Please note the manuscript has yet to be formally accepted for publication. Subsequent versions of this manuscript may have slightly different content. If accepted, the final version of this manuscript will be available via the 'Peer-reviewed Publication DOI' link on the right-hand side of this webpage. Please feel free to contact any of the authors; we welcome feedback.

A Phanerozoic Atlas of Earth's Atmosphere, Surface, and Interior Derived from the PANALESIS Plate Tectonic Model

Florian Franziskakis[1] Niklas Werner*[2] Christian Vérard[3]
Sébastien Castelltort[3] Grégory Giuliani[1]

[1]Institute for Environmental Sciences, University of Geneva, Switzerland
{florian.franziskakis, gregory.giuliani}@unige.ch
[2]Department of Earth and Planetary Sciences, ETH Zürich, Switzerland
niklas.werner@eaps.ethz.ch
[3]Department of Earth Sciences, University of Geneva, Switzerland
{christian.verard, sebastien.castelltort}@unige.ch

*Corresponding author: niklas.werner@eaps.ethz.ch

Abstract

Reconstructing the Earth system evolution through deep time requires spatially consistent, multi-layer datasets that integrate geological, geophysical, and climatic information. Here we present a unified, high-resolution (10×10 km) global dataset describing the Earth's evolution over the past 545 million years. This atlas provides 45 time slices spanning the Phanerozoic, each including quantified palaeogeography, seafloor age, crustal thickness, lithospheric thickness, and climate variables (surface air temperature, precipitation, and climate zones). All layers are generated using a consistent reconstruction framework based solely on the PANALESIS plate tectonic model, ensuring self consistency and reproducibility across the entire record.

Surface and interior layers are computed from physically based relationships linking palaeogeography, crustal structure, tectonic domain boundaries, and seafloor thermal evolution. Climate simulations are produced using the intermediate complexity AOGCM PLASIM–GENIE, forced by time-dependent palaeogeography, atmospheric CO2, and solar luminosity. Technical validation against present-day reference datasets demonstrates strong agreement for seafloor age, palaeogeography, and crustal structure, and captures first-order spatial patterns in lithospheric thickness and climate fields.

This atlas enables a broad range of applications, including paleoclimate modelling, biodiversity and biogeographic analyses, tectonic and geodynamic studies, and long-term surface process mod-

elling. All datasets and code are openly available, ensuring transparent reuse and straightforward integration into Earth system modelling and Geographic Information Systems (GIS) workflows. The PANALESIS Atlas establishes a comprehensive, fully quantified baseline for investigating Earth's coupled surface–interior–atmosphere evolution across the Phanerozoic.

1 Background & Summary

Reconstructing the Earth's surface evolution over geological timescales is fundamental for understanding long-term Earth system dynamics. The spatial configuration of continents and oceans influences global climate[1,2], ocean circulation and temperature[3–6] or biodiversity patterns[7]. Reconstructions of past environments enable researchers to explore questions ranging from the drivers of mass extinctions to the mechanisms behind major climate transitions. At the core of these reconstructions are global plate tectonic models, which synthesize geological, geophysical, and paleontological evidence to describe the motion and interaction of tectonic plates over hundreds of millions of years[8–13].

Palaeogeographic maps derived from these models are useful tools for Earth scientists, as they provide spatial frameworks for investigating global sea-level variations[14–17], modelling ancient climates[18,19], and tracing the evolution of life through deep time[20–23]. Beyond academic research, palaeogeography also supports applied domains such as hydrocarbon exploration or mineral prospecting[24]. The ability to link geological history with climate and biogeochemical models depends on the availability of consistent and quantified reconstructions.

Existing palaeogeographic datasets, such as the ones from the PALEOMAP project[10], the PANALESIS model[15,25,17], or other sources[9,16] differ considerably in scope, resolution, and methodological foundations. Many published maps are generated under distinct reconstruction methodologies, leading to differences in how coastlines, ocean basins, or continental regions are represented through time. In numerous cases, palaeotopography is provided at coarse resolution (i.e. 1°x1°), or expressed qualitatively, with limited constraints on crustal structure, lithospheric domains, or the age of oceanic basins. Time slices are often generated independently, meaning that long-term continuity in surface evolution is not always explicitly maintained[26]. Furthermore, additional components of the Earth system are not systematically included directly together with palaeogeography, but are building on it in subsequent studies, as it is the case for drainage networks and sediment-routing patterns[27], or seafloor age[28].

This dataset extends the existing PANALESIS palaeogeographic maps into a unified Earth system atlas. The PANALESIS Atlas provides a comprehensive, high-resolution dataset capturing Phanerozoic Earth evolution across 45 time steps (545 Ma–present). At 10 × 10 km resolution, it includes global raster layers of palaeogeography, seafloor age, crustal thickness, and lithospheric thickness. Climate simulations (temperature, precipitation) and derived Köppen-Geiger climate zones, all computed using the palaeogeographic maps as boundary conditions are also included, allowing for long-term, coupled

geodynamics, surface and climate understanding of the Earth system (Fig. 1).

2 Methods

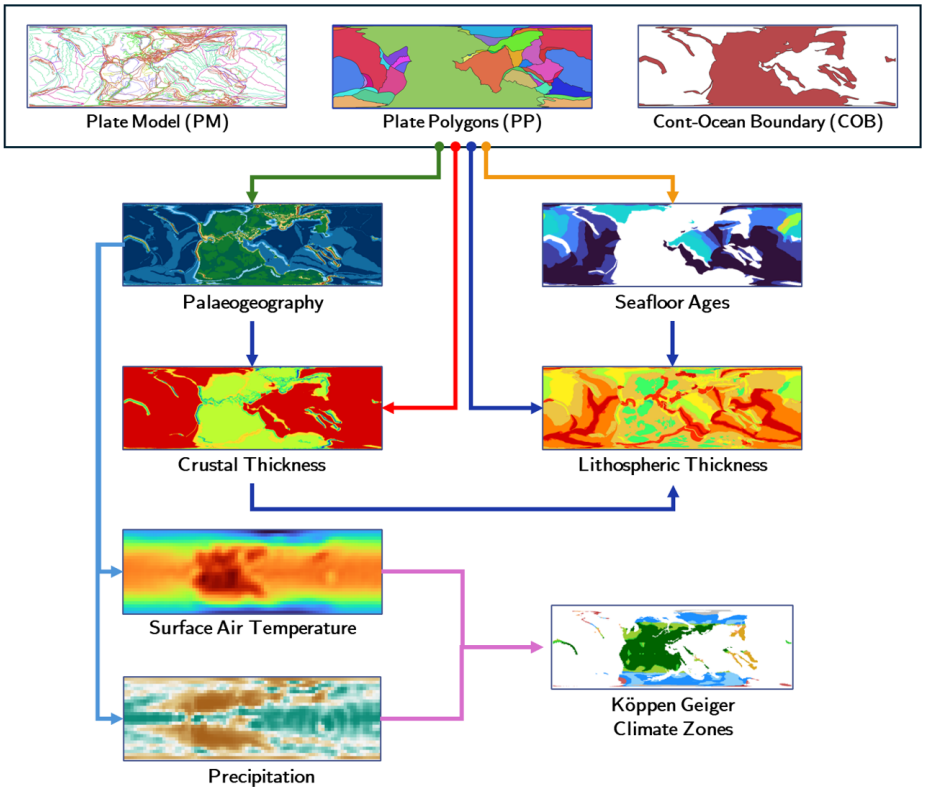

Figure 1: Atlas products creation workflow, with maps from the 250 Ma reconstruction used to illustrate the workflow. From the original PANALESIS model's three main layers (i) Plate Model (PM) lines describing geodynamic environments, (ii) Plate Polygons (PP) representing the tectonic plates, and the Continent-Ocean Boundary (COB) discriminating between oceanic and continental crust. First, the palaeogegoraphy is created with TopoChronia[29] using the PM, PP and COB. Seafloor ages maps are also created using the PANALESIS model inputs. Crustal thickness is based on the palaeogeography and model inputs, and is in turn used to derived the lithospheric thickness (together with the model inputs and seafloor ages maps). Climate outputs (surface air temperature and precipitation) are created using the PLASIM-GENIE model[30] with palaeogeographic maps as boundary conditions. The climate outputs are finally combined into Köppen-Geiger climate zones.

2.1 Palaeogeography

Palaeogeographic maps (Fig. 2) were generated using the PANALESIS plate model[15,25,31], which comprises (i) plate polygons, delineating the tectonic plates boundaries, (ii) polygons marking the boundary between continental and oceanic crust (COB), with the inside of the polygon indicating continental crust, and (iii) lines delineating typical geodynamic environments such as zones of subduction, collision, passive margins, mid-oceanic ridges, isochrons, hot-spots, cratons or rifts. The detailed methodology to generate these maps has already been published in references above, and the software is openly avail-

able and described in Franziskakis et al.[29], helping to quantify the sea-level evolution throughout the Phanerozoic[17].

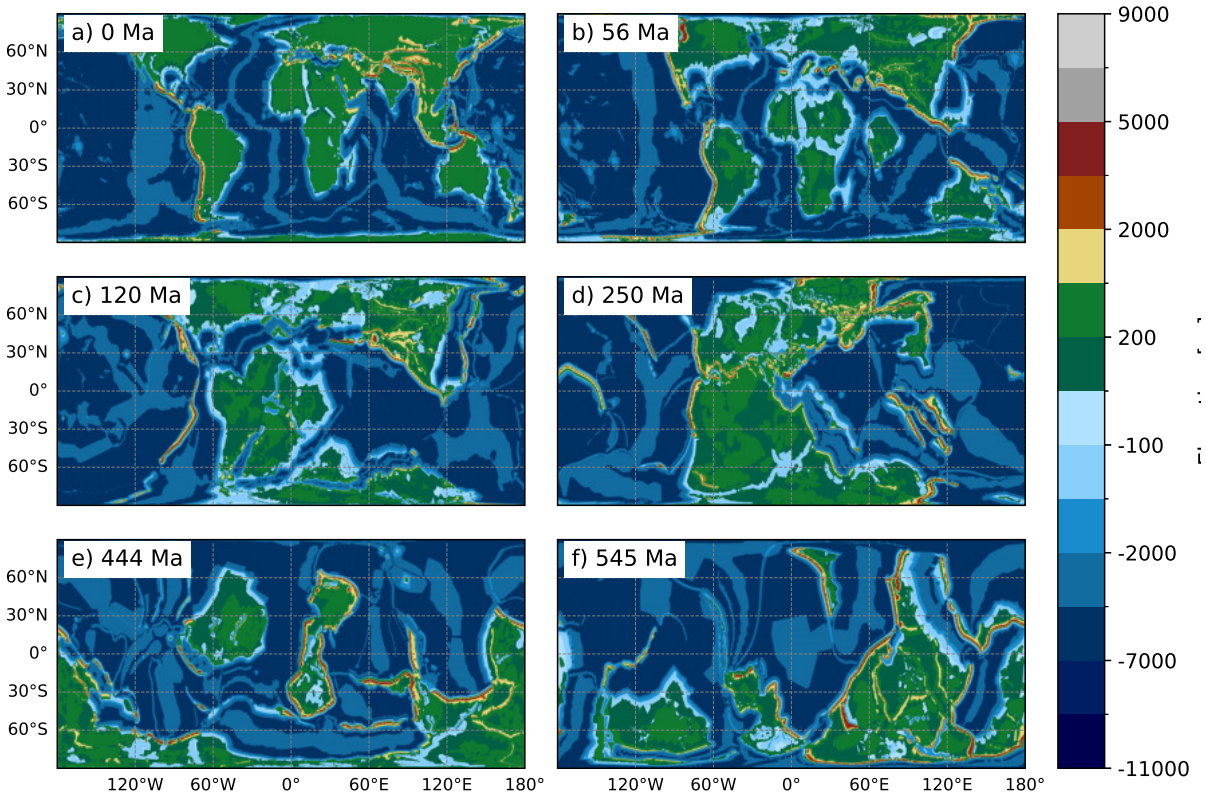

Figure 2: Selected timeslices for palaeogeography: 0 Ma (Quaternary), 56 Ma (Paleogene), 120 Ma (Cretaceous), 250 Ma (Permian–Triassic boundary), 444 Ma (Ordovician–Silurian boundary), and 540 Ma (Ediacaran–Cambrian boundary). The elevation is expressed in meters and already accounts for sea-level variations, assuming constant oceanic volume through time.

2.2 Seafloor ages

The seafloor age maps (Fig. 3) are generated using the plate model, the plate polygons and the COB. For each reconstruction, we first delineate oceanic basins, by selecting the lines representing mid-oceanic ridges, isochrons and passive margins.

We then process these lines plate by plate by keeping only the lines intersecting each plate polygon. We extract the vertices from each line and calculate their feature age as the difference between the absolute age of the line and the reconstruction age. We also extract the plate polygon vertices and assign them the feature age of the nearest line vertex.

For each plate, a raster is interpolated from the merged vertices using a Triangulated Irregular Network (TIN) with linear barycentric interpolation, implemented via `scipy.interpolate.LinearNDInterpolator`[32]. The algorithm first constructs a Delaunay triangulation over the sample points using the Qhull library[33], which implements the Quickhull algorithm for convex hulls and derives Delaunay triangulations as a by-product via projective lifting. Each output pixel is then assigned the value obtained by linearly in-

terpolating within the enclosing triangle using barycentric coordinates. Pixels falling outside the convex hull of the sample points are assigned a no-data value of −9999, which are subsequently filled using GDAL's `FillNodata`[34] with a maximum search distance of 150 pixels. The age value for each pixel $A(x)$ is calculated as:

$$A(x) = \sum_{i=1}^{3} \lambda_i \, z_i \tag{1}$$

where z_i is the age (in Myr) at vertex i of the enclosing Delaunay triangle, and λ_i are the barycentric coordinates of location x with respect to that triangle, satisfying $\lambda_i \geq 0$ and $\sum_{i=1}^{3} \lambda_i = 1$.

We then remove pixels located inside the continent-ocean boundary to keep pixels strictly inside the plate, preventing overlapping with boundary lines. All rasters are then mosaicked into a single global layer for each reconstruction. Since pixels are kept strictly inside plate boundaries to avoid overlaps, gaps may be present at plate junctions. We fill these gaps using nearest neighbour interpolation and perform a final clip to exclude pixels inside continents that might have been created by the gap filling step.

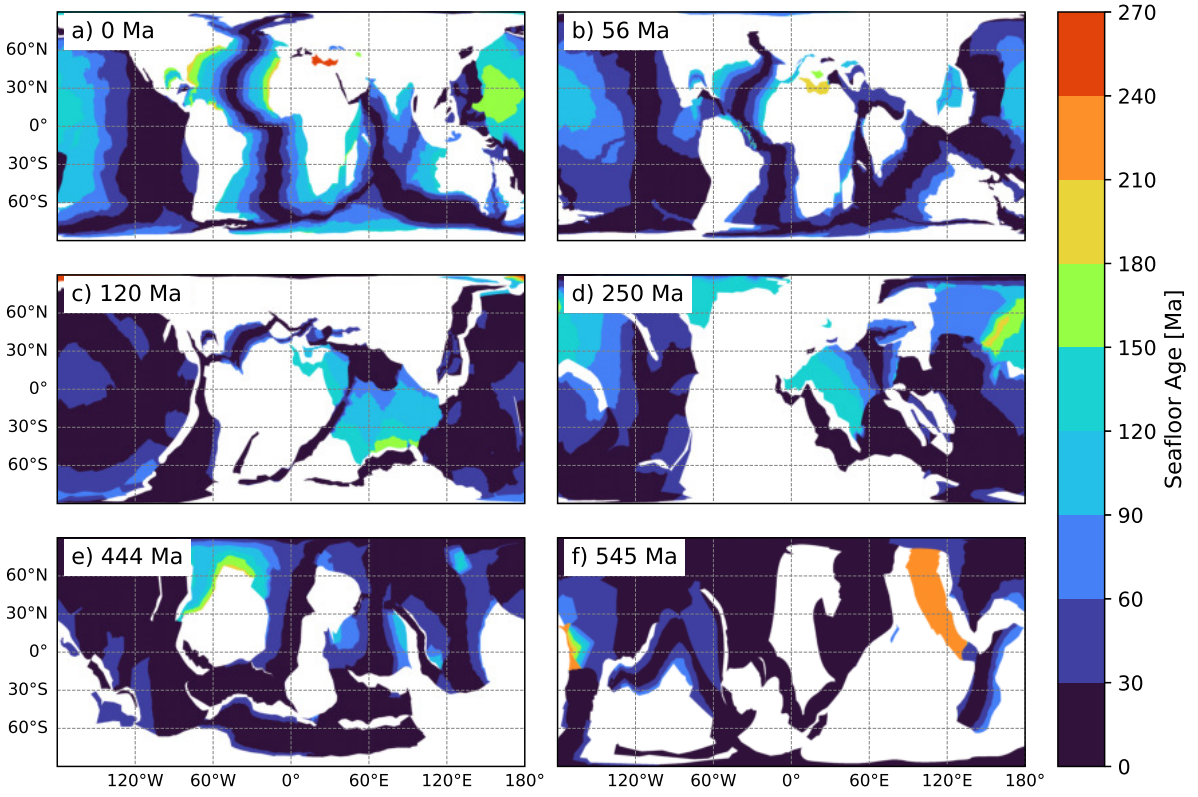

Figure 3: Selected timeslices for seafloor age: 0 Ma (Quaternary), 56 Ma (Paleogene), 120 Ma (Cretaceous), 250 Ma (Permian–Triassic boundary), 444 Ma (Ordovician–Silurian boundary), and 540 Ma (Ediacaran–Cambrian boundary). Age is expressed in millions of years. No-data pixels indicate areas where there is no seafloor (continental crust) and are displayed in white.

The global rasters are finally reprojected to a world cylindrical equal area projection to fit the same

extent and pixel size as the palaeogeographic maps.

2.3 Crustal thickness

The crustal thickness maps (Fig. 4) are generated using the palaeogeographic maps and the COB polygon, which delineates continental regions, with areas inside the polygon representing continental crust and areas outside representing oceanic crust. The crustal thickness (in km) for each pixel is determined based on whether the pixel is located within oceanic or continental domains, as defined by the COB polygon, and for continental pixels, on the elevation value. These maps represent the strict thickness of the crust without sediments, and without ice or water above. They do not represent the depth of the boundary between the crust and the upper mantle.

For oceans, we define a fixed thickness of 6.5 km, following the CRUST 2.0 model approach for crustal thickness without sediments[35]. For continents, the thickness depends on elevation via a power-law relationship constrained by three geologically constrained reference points: 6.5 km at −2000 m (oceanic baseline at the continent-ocean transition as defined in CRUST 2.0), 37 km at 240 m (global mean continental elevation and thickness) after Cawood *et al.*[36] and Vérard *et al.*[37], and 80 km at 9000 m (maximum crustal root beneath the Himalayas)[38,39]. A power law is preferred over a piecewise linear fit because it is smooth and strictly monotonic and avoids an artificial kink at the mean continental reference point. The crustal thickness for each pixel $T_C(x)$ is therefore:

$$T_C(x) = \begin{cases} 6.5, & \text{if not COB (Oceanic)} \\ 6.5, & \text{if COB and } E(x) \leq -2000 \\ 0.4292\,(E(x)+2000)^{0.5527} + 6.5, & \text{if COB and } -2000 < E(x) < 9000 \\ 0.002407789353\,E(x) + 58.38269138, & \text{if COB and } E(x) \geq 9000 \\ 0, & \text{otherwise} \end{cases} \tag{2}$$

where $E(x)$ is the elevation sampled from the palaeogeographic map (in m) and COB is a Boolean mask for continents (True = inside continent, False = outside). The power-law branch passes exactly through all three reference points, with full coefficients $a = 0.4291976178$ and $b = 0.5526881969$.

2.4 Lithospheric thickness

Lithospheric thickness (Fig. 5) is computed from crustal thickness $T_C(x)$, seafloor age $A(x)$, and the tectonic domain masks: COB (continent-ocean boundary), CRA (craton), and RIB (rift/basin age). For any given pixel x, the lithospheric thickness $T_L(x)$ is calculated as:

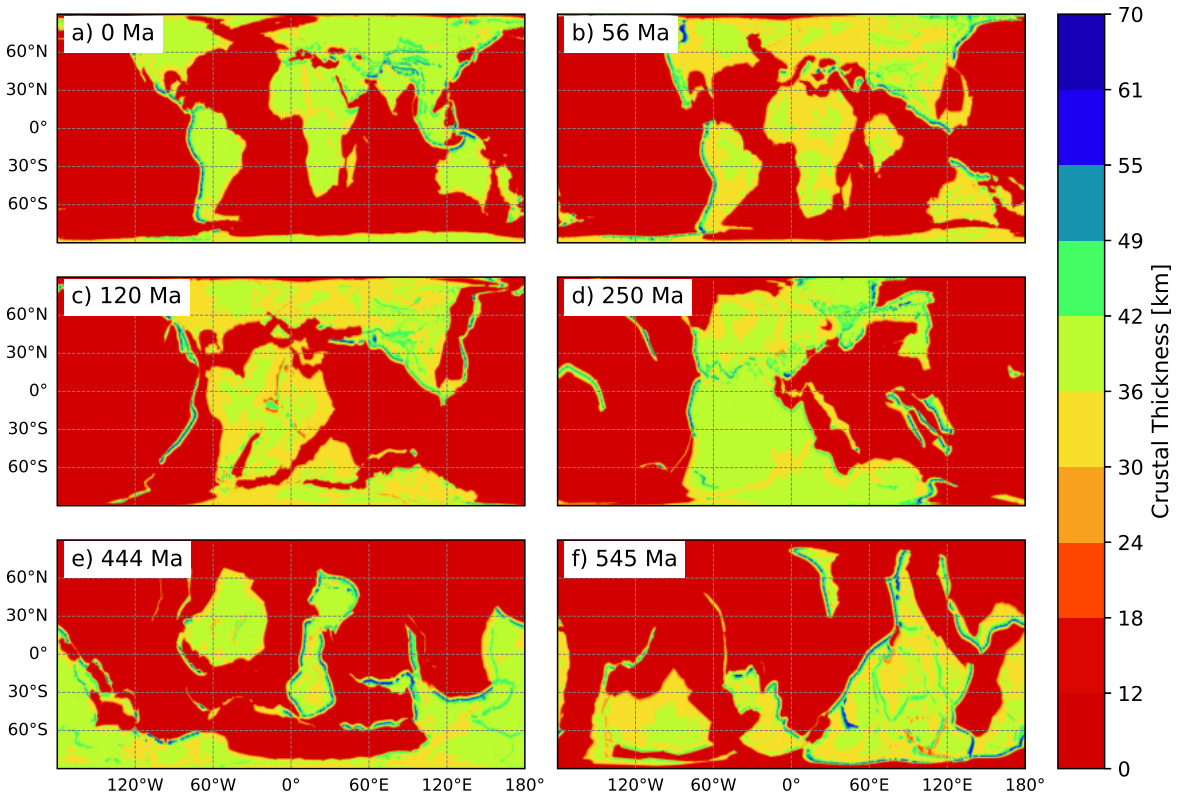

Figure 4: Selected timeslices for crustal thickness: 0 Ma (Quaternary), 56 Ma (Paleogene), 120 Ma (Cretaceous), 250 Ma (Permian–Triassic boundary), 444 Ma (Ordovician–Silurian boundary), and 540 Ma (Ediacaran–Cambrian boundary). The values are expressed in kilometers.

$$
T_L(x) = \begin{cases}
T_C(x) + 2 \times 1.338\sqrt{22.94 \times A(x)}, & \text{if } \neg COB \text{ (oceanic)}, \\
95, & \text{if } COB \wedge T_C(x) \leq 30 \text{ km}, \\
3\,T_C(x), & \text{if } COB \wedge \neg CRA \wedge \neg RIB \text{ (normal continental)}, \\
5\,T_C(x), & \text{if } COB \wedge CRA \wedge \neg RIB \text{ (cratonic)}, \\
\left(0.75 + \text{clip}\left(\dfrac{R(x)}{100}, 0, 1\right)\right) T_C(x), & \text{if } COB \wedge \neg CRA \wedge RIB \text{ (rifted)}, \\
2.5\,T_C(x), & \text{if } COB \wedge CRA \wedge RIB \text{ (ambiguous/overlapping)},
\end{cases} \tag{3}
$$

where $T_C(x)$ is the crustal thickness (km), $A(x)$ is the seafloor age (Ma), $R(x)$ is the rift age (Myr), and COB, CRA, and RIB are Boolean masks. The mask RIB indicates the presence of rift/basin domains, i.e.,

$$RIB(x) = \begin{cases} \text{True}, & \text{if } R(x) \text{ is defined,} \\ \text{False}, & \text{if } R(x) = \text{NaN.} \end{cases} \tag{4}$$

The formulation above reflects the differing thermal and tectonic controls on lithospheric thickness in oceanic, continental, cratonic and rifted settings.

For oceanic regions ($\neg COB$), lithospheric thickness is computed from a half-space cooling model of the form $T_L = T_C + 2\eta\sqrt{\kappa t}$, using a thermal diffusivity of $\kappa = 22.94$ km^2/Ma and an effective similarity constant $\eta = 1.338$. This formulation is consistent with the classical error-function solution to the conductive cooling of newly formed oceanic plates[40–42]. At the transition between oceanic and continental lithosphere, we assign a fixed 95 km thickness value to replace no-data pixels that are located on the boundary line of the continent-ocean boundary (COB) layer, defined in our formula as pixels where crustal thickness is thinner than 30 km.

Inside the COB, the thermal structure is no longer governed primarily by age-dependent cooling but instead by long-term tectonic history and crustal architecture. Continental lithosphere is parameterised using simple multiplicative relationships that scale lithospheric thickness with crustal thickness: a factor of 3 for normal continental lithosphere and a factor of 5 for cratonic regions. These coefficients of 3 and 5 lie within the commonly observed range of crust–LAB correlations in global models[43–45], and reflect the greater thermal stability and compositional buoyancy of cratonic keels respectively[46,47].

Rift and basin domains are treated separately through an age-dependent scaling. The lithosphere is shallower immediately after rifting and progressively thickens with time. This behaviour is represented by a multiplier ranging from 0.75 (for very young rifts) to 1.75 (for rifts older than 100 Myr), consistent with the idea that rifting zone create thinned lithosphere for early ages of rifting[48–51]. Pixels classified simultaneously as cratonic and rifted (ambiguous domains) are assigned an intermediate scaling factor of 2.5, reflecting their transitional characteristics and the difficulty of resolving LAB geometry in such settings.

2.5 Climate simulation dataset for the Phanerozoic

2.5.1 Near Surface Air Temperature and Precipitation

We provide a set of global palaeoclimate simulation outputs designed to accompany the palaeogeographic reconstructions presented in this atlas. The dataset comprises gridded fields of near-surface air temperature (Fig. 6), precipitation (Fig. 7), and derived Köppen–Geiger climate classifications (Fig. 8) for a suite of discrete Phanerozoic time slices. These data are intended for use as initial conditions, comparative benchmarks, or forcing inputs in downstream palaeoclimate, palaeoecological, and Earth system

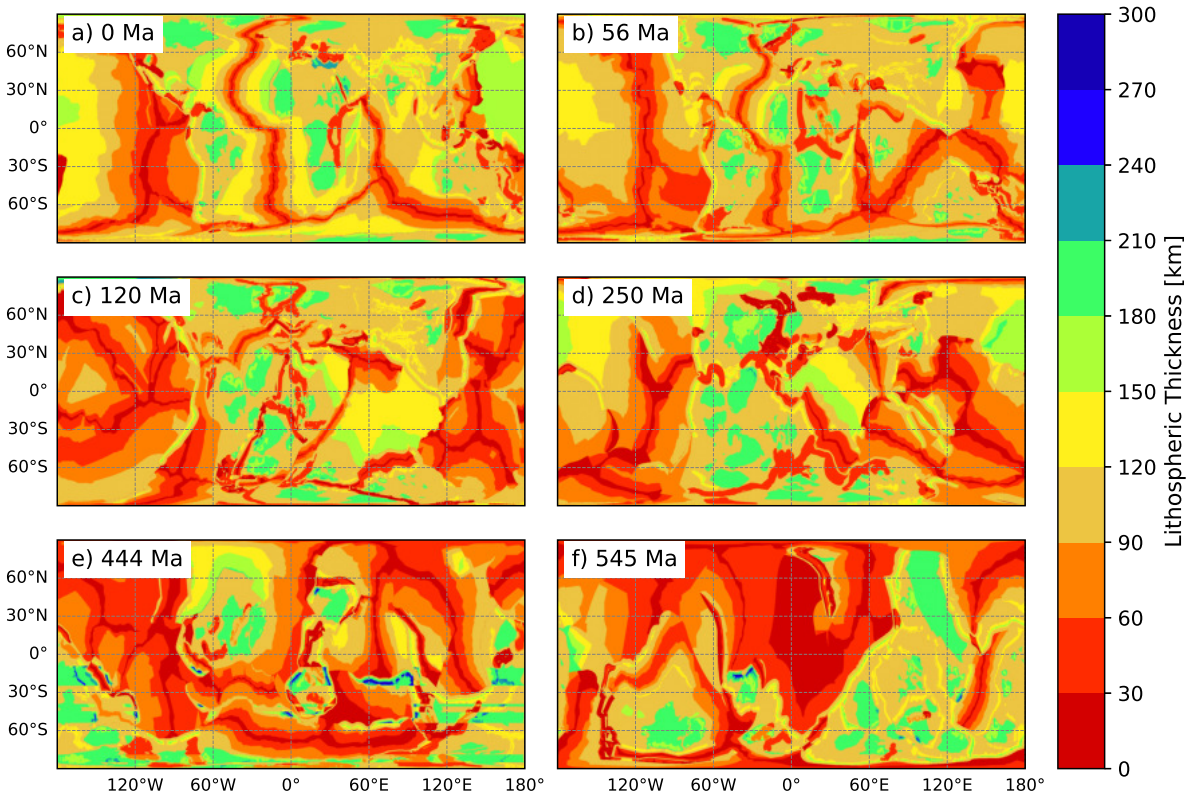

Figure 5: Selected timeslices for lithospheric thickness: 0 Ma (Quaternary), 56 Ma (Paleogene), 120 Ma (Cretaceous), 250 Ma (Permian–Triassic boundary), 444 Ma (Ordovician–Silurian boundary), and 540 Ma (Ediacaran–Cambrian boundary). The thickness is expressed in kilometers.

analyses.

All simulations were performed using the intermediate-complexity PlaSim–GENIE climate model[30], which couples the Planet Simulator atmospheric general circulation model (PlaSim; Fraederich *et al.*[52]) to the GOLDSTEIN dynamic ocean and sea-ice components of the GENIE Earth system framework. This configuration resolves atmosphere–ocean–sea-ice interactions in a physically consistent yet computationally efficient manner, enabling multi-millennial integrations across a large number of palaeogeographic scenarios. The atmospheric component was operated at a spectral resolution equivalent to T21, coupled to an ocean model of matching horizontal resolution with 16 vertical layers.

Atmospheric carbon dioxide concentrations (pCO_2) were prescribed for each time slice using the COPSE Phanerozoic CO_2 reconstruction from Lenton *et al.*[53]. This forcing was selected to ensure internal consistency, as the COPSE model does not rely on external palaeogeographic reconstructions. Solar luminosity was adjusted as a function of geological time following the formulation of Gough[54]. All other model parameters were kept constant across simulations.

The GENIE land surface and vegetation module (ENTS) was modified to reflect the absence or limited extent of terrestrial vegetation during early Phanerozoic intervals. For simulations older than 380 Ma, the vegetation module was disabled. For time slices between 440 and 380 Ma, land surface

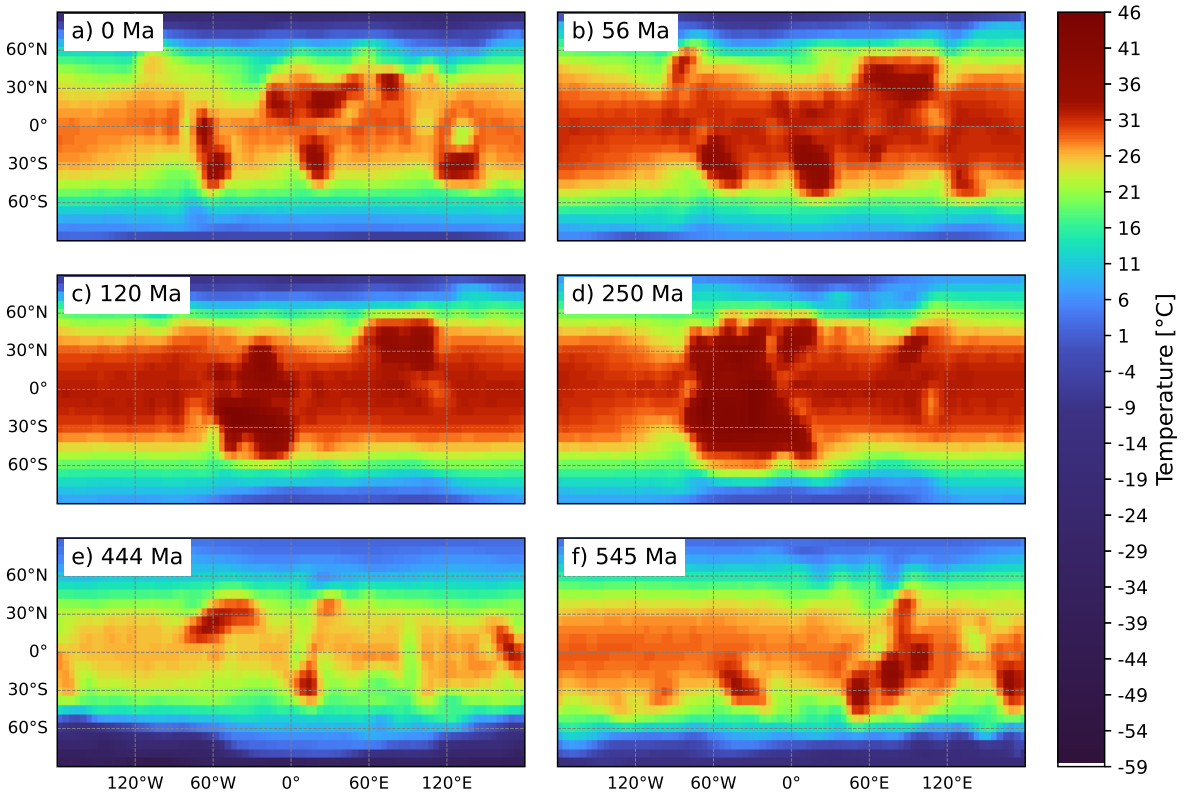

Figure 6: Selected timeslices for temperature: 0 Ma (Quaternary), 56 Ma (Paleogene), 120 Ma (Cretaceous), 250 Ma (Permian–Triassic boundary), 444 Ma (Ordovician–Silurian boundary), and 540 Ma (Ediacaran–Cambrian boundary). The temperature is expressed in °C.

properties were prescribed with a broadband albedo of 0.205 and a surface roughness length of 0.1 m to represent basal embryophyte-dominated landscapes, following Le Hir et al.[55] and Pohl et al.[56]. For time slices earlier than 440 Ma, continental surfaces were parameterized as non-vegetated rocky deserts, with an albedo of 0.32 and a roughness length of 0.05 m. For each simulation, monthly mean near-surface air temperature and precipitation fields were archived on the native model grid.

2.5.2 Derivation of Köppen–Geiger climate classifications

Köppen–Geiger climate classifications were derived from the simulated monthly near-surface air temperature and precipitation fields following the threshold-based methodology described by Pohl et al.[56], applied consistently across all Phanerozoic time slices. Monthly temperature and precipitation outputs from the PlaSim–GENIE simulations were first standardized to a common month–latitude–longitude coordinate structure. Precipitation fluxes were converted to monthly totals (mm $month^{-1}$) assuming a 360-day calendar consistent with the climate model configuration.

For each grid cell, standard Köppen-Geiger diagnostic variables were computed, including mean annual temperature and precipitation, temperature of the warmest and coldest months, total summer and winter precipitation, and precipitation of the driest and wettest months. Hemispheric seasonality was accounted for by defining boreal summer as April–September in the Northern Hemisphere and

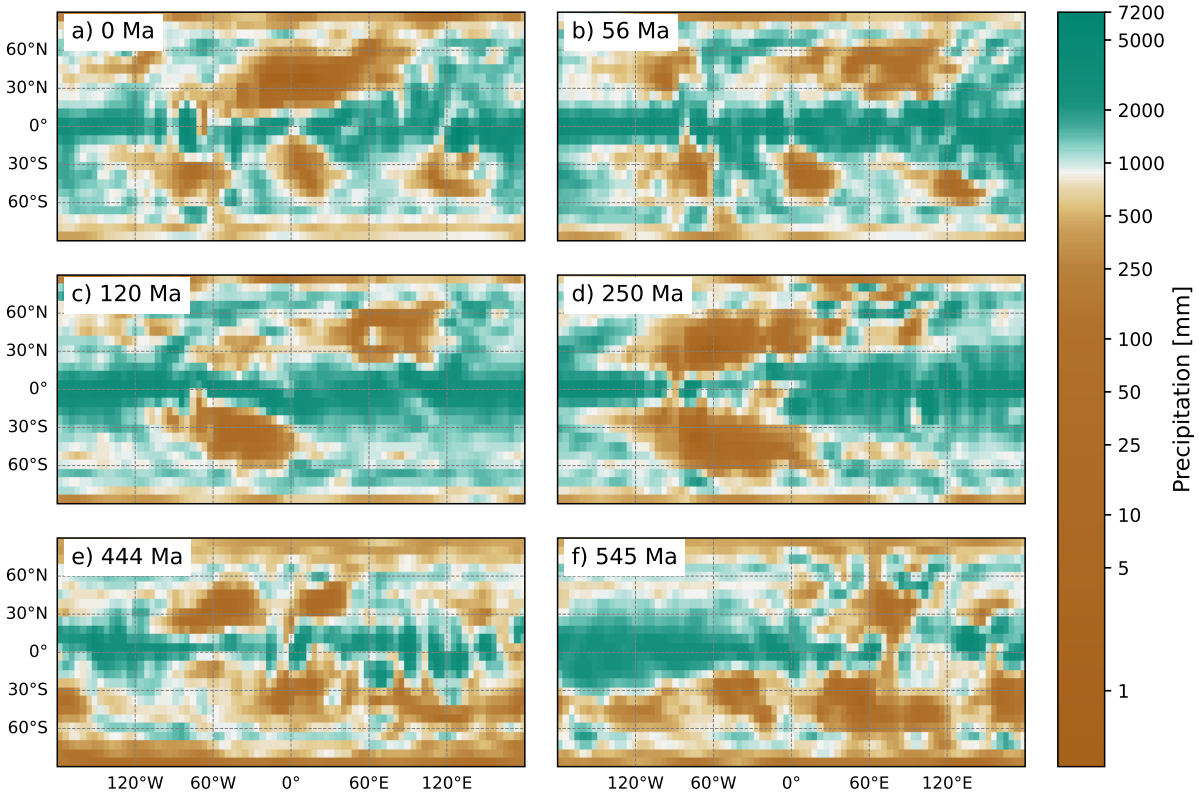

Figure 7: Selected timeslices: 0 Ma (Quaternary), 56 Ma (Paleogene), 120 Ma (Cretaceous), 250 Ma (Permian–Triassic boundary), 444 Ma (Ordovician–Silurian boundary), and 540 Ma (Ediacaran–Cambrian boundary). The precipitation is expressed in millimeters per year.

October–March in the Southern Hemisphere, with the inverse applied for winter. Arid (B-type) climates were identified first using the Köppen aridity threshold formulation prior to assignment of tropical (A), temperate (C), cold (D) or polar (E) types.

To reduce visual aliasing associated with the relatively coarse native model grid, monthly temperature and precipitation fields were bilinearly interpolated to a finer grid prior to classification. Köppen–Geiger classes were then computed on this supersampled grid, following a categorical assignment scheme based on the computed climate indices. This procedure improves the spatial coherence of climate zone boundaries while preserving the underlying large-scale climate signal.

Land–sea masking was applied after supersampling using time-slice-specific palaeogeographic coastlines. Land masks were generated from vector shoreline reconstructions by rasterizing land polygons onto the supersampled grid, ensuring that Köppen–Geiger classifications were retained only over continental areas and excluded from oceanic regions. The final output consists of categorical Köppen–Geiger climate maps for each time slice, provided on a regular latitude–longitude grid and intended for visualization, comparison with proxy data, and reuse in downstream palaeoclimate and palaeoenvironmental analyses.

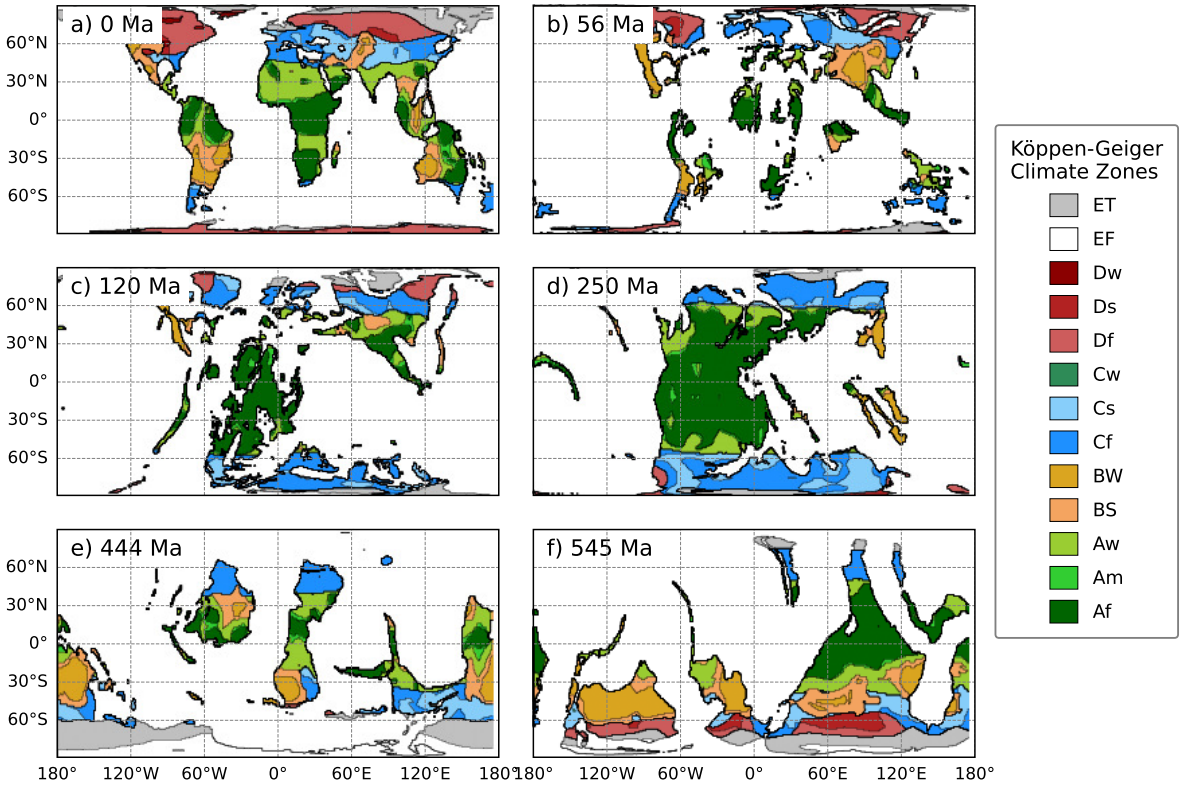

Figure 8: Selected timeslices for Köppen-Gerîger Climate Zones: 0 Ma (Quaternary), 56 Ma (Paleogene), 120 Ma (Cretaceous), 250 Ma (Permian–Triassic boundary), 444 Ma (Ordovician–Silurian boundary), and 540 Ma (Ediacaran–Cambrian boundary). The classes are defined by the two-letter scheme.

3 Data Record

All datasets generated for the PANALESIS Atlas are publicly available under the title *"A Phanerozoic Atlas of Earth's Atmosphere, Surface, and Interior Derived from the PANALESIS Plate Tectonic Model"* with DOI: https://doi.org/10.5281/zenodo.19134591. The unified release, titled , includes maps described in this manuscript, in their original cylindrical equal area projection (ESRI:54034) named "EqualArea" in the data record, and in degrees (EPSG:4326), named "LatLong" in the data record.

The LatLong maps have decimal degrees (°) units, with a 0.1°x0.1° resolution. The bounds are: xmin:-180.0 ymin:-90.0 xmax:180.0 ymax:90.0

The EqualArea maps have meters units, with a 10x10 km resolution. The projected bounds are: xmin: -20037508.34 ymin:-6363885.33 xmax:20037508.34 ymax:6363885.33, corresponding to the same extent as the LatLong maps.

Data are distributed under a Creative Commons Attribution (CC BY 4.0) license.

The dataset provides the following global maps:

1. Palaeogeography, expressed in meters [m]

2. Seafloor age, expressed in millions of years [Myr]

3. Crustal thickness, expressed in kilometers [km]

4. Lithospheric thickness, expressed in kilometers [km]

5. Air surface temperature, expressed in degrees Celsius [°C]

6. Precipitation, expressed in millimeters per year [mm/yr]

7. Köpen-Geiger climate zones (KGCZ), described by the two-letter classification code

Each type of map is available for 45 geological time steps from 000 to 545 Ma: `000, 006, 011, 015, 020, 033, 040, 048, 056, 068, 084, 094, 100, 113, 120, 133, 140, 154, 165, 180, 200, 210, 220, 230, 240, 250, 270, 290, 300, 315, 331, 350, 370, 383, 393, 408, 420, 444, 463, 475, 489, 500, 518, 535, 545`.

The Zenodo record is organized as follows:

```
PANALESIS_Atlas_v1.0/
|-- README_PANALESIS_Atlas_v1.0.txt
|-- license.txt
|-- EqualArea/
|   |-- palaeogeography/
|   |-- seafloor_age/
|   |-- crustal_thickness/
|   |-- lithospheric_thickness/
|   |-- precipitation/
|   |-- air_surface_temperature/
|   `-- climate_zones/
`-- LatLong/
    |-- palaeogeography/
|   |-- seafloor_age/
|   |-- crustal_thickness/
|   |-- lithospheric_thickness/
|   |-- precipitation/
|   |-- air_surface_temperature/
|   `-- climate_zones/
```

4 Technical Validation

We validate the PANALESIS Atlas products against established present-day reference datasets using a multi-scale, quantitative approach. Validation is conducted for all variables with the exception of KGCZ:

palaeogeography, seafloor age, crustal thickness, lithospheric thickness, near surface air temperature, and precipitation. All comparisons are performed at the global scale (entire map), as well as on continental areas, and oceans only, as defined by the extent of the COB polygon. Validation is performed at the native 10 km resolution for palaeogeographic and seafloor ages maps, given the comparison data is available at this high resolution. The crustal and lithospheric thickness maps are compared at a 200 km resolution to match the reference data and avoid downsampling it. Finally, the climate outputs are compared at 500 km resolution given the PLASIM-GENIE model low resolution.

4.1 Reference Datasets

Validation datasets include: (i) the ETOPO 2022 global relief model[57] that has an original resolution of 15 arc second, here resampled to an equal area grid of 10 by 10 km, (ii) the global seafloor age grids of Müller et al.[58] and Seton et al.[59] resampled to a resolution of 10 by 10 km, (iii) the CRUST 2.0 model[35] and (iv) the LITHO 1.0 model[60], CAM2016[61,62] and LithoRef18[63], all with original resolutions between 1 and 2.5° resampled (using an average mean of pixels) to an equal area grid of 200 by 200 km. These represent community standards for present-day topography, oceanic crustal age, and crustal/lithospheric structure. Beyond resolution, all reference datasets were resampled to match the spatial projection and pixel alignment of PANALESIS grids prior to analysis.

4.2 Metrics

For each variable we compute statistics of the reference model versus our maps. We first compute: root mean square error (RMSE),

$$\mathrm{RMSE} = \sqrt{\frac{1}{n}\sum_{i=1}^{n}(y_i - \hat{y}_i)^2} \tag{5}$$

mean bias,

$$\mathrm{Bias} = \frac{1}{n}\sum_{i=1}^{n}(y_i - \hat{y}_i) \tag{6}$$

mean absolute error (MAE),

$$\mathrm{MAE} = \frac{1}{n}\sum_{i=1}^{n}|y_i - \hat{y}_i| \tag{7}$$

Pearson correlation coefficient (r),

$$r = \frac{\sum_{i=1}^{n}(y_i - \bar{y})(\hat{y}_i - \bar{\hat{y}})}{\sqrt{\sum_{i=1}^{n}(y_i - \bar{y})^2}\sqrt{\sum_{i=1}^{n}(\hat{y}_i - \bar{\hat{y}})^2}} \tag{8}$$

and coefficient of determination (R^2),

$$R^2 = 1 - \frac{\sum_{i=1}^{n}(y_i - \hat{y}_i)^2}{\sum_{i=1}^{n}(y_i - \bar{y})^2} \tag{9}$$

For which y_i are the reference dataset values, $\hat{y}_i$ are the predicted (modeled) values, $\bar{y}$ and $\bar{\hat{y}}$ are their respective means, and n is the number of observations. We also quantify distribution similarity using the Wasserstein distance (Earth Mover's Distance)[64–66], which measures overall distributional offset in physical units.

$$W_1(P, Q) = \inf_{\gamma \in \Pi(P,Q)} \int_{\mathbb{R}\times\mathbb{R}} |x - y| \, \mathrm{d}\gamma(x, y) \tag{10}$$

where P and Q are the reference and predicted distributions respectively, and $\Pi(P, Q)$ denotes the set of all joint distributions with marginals P and Q.

To assess model skill beyond simple correlation, we compute the Index of Agreement (IoA)[67], a standardized measure of model accuracy ranging from 0 to 1.

$$\mathrm{IoA} = 1 - \frac{\sum_{i=1}^{n}(y_i - \hat{y}_i)^2}{\sum_{i=1}^{n}\left(|\hat{y}_i - \bar{y}| + |y_i - \bar{y}|\right)^2} \tag{11}$$

The Kolmogorov-Smirnov (K-S) statistic[68,69]tests whether model and reference distributions differ significantly,

$$D_{KS} = \sup_x |F_P(x) - F_Q(x)| \tag{12}$$

where F_P and F_Q are the empirical cumulative distribution functions of the reference and predicted distributions respectively. We additionally report Spearman's rank correlation (ρ)[70],

$$\rho = 1 - \frac{6\sum_{i=1}^{n} d_i^2}{n(n^2 - 1)} \tag{13}$$

where $d_i = \mathrm{rank}(y_i) - \mathrm{rank}(\hat{y}_i)$ is the difference between the ranks of each observation pair, alongside

Pearson's r to detect non-linear relationships: where $\rho > r$, the model captures monotonic topographic patterns despite potential scaling biases; where $r > \rho$, non-monotonic errors may be present.

4.3 Palaeogeography

Present-day palaeogeography from the PANALESIS Atlas is validated against ETOPO 2022 [57] at 10 km resolution across 5.09 million valid pixels (Table 1). Globally, the model achieves an RMSE of 950 m with minimal mean bias of −25.1 m (−0.89%), indicating negligible systematic vertical offset. The model exhibits strong linear correlation (Pearson $r = 0.92$, $R^2 = 0.85$) and high predictive skill (Index of Agreement = 0.96), substantially exceeding the performance of a simple mean-value baseline. Half of all pixels show absolute errors below 375 m, with 90% below 1497 m, demonstrating robust agreement across most of the globe. The Wasserstein distance of 177 m reflects modest distributional offset relative to the 15,636 m range in observed elevations. Regional performance varies by tectonic domain. In continental regions (2.03 million pixels), the model shows moderate correlation ($r = 0.54$, $R^2 = 0.20$) with RMSE of 1057 m and mean bias of −38.1 m. The notable difference between Pearson ($r = 0.54$) and Spearman ($\rho = 0.45$) correlations suggests non-monotonic errors, likely reflecting challenges in capturing steep continental relief and inland basin geometries. In oceanic regions (3.06 million pixels), performance is stronger with RMSE of 871 m, minimal bias (−16.5 m, −0.39%). Here, Spearman correlation ($\rho = 0.70$) exceeds Pearson ($r = 0.63$), indicating the model successfully captures monotonic depth patterns despite some non-linear scaling differences, consistent with plate cooling dynamics. Median absolute errors are comparable between continental (355 m) and oceanic (386 m) domains, though extreme errors (99th percentile: 3933 m continental vs. 3192 m oceanic) are higher on continents due to steep topographic gradients. These results demonstrate that the PANALESIS plate tectonic reconstruction successfully reproduces first-order global bathymetric and topographic patterns, with particularly strong performance in oceanic basins where plate cooling models dominate. Continental elevation prediction remains more challenging, reflecting known limitations in modelling dynamic topography, erosion, and sedimentary basin subsidence from plate kinematic constraints alone.

4.4 Seafloor Age

Present-day seafloor age from the PANALESIS Atlas is validated against the global seafloor age grid of Seton et al. [59] at 10 km resolution across 2.88 million oceanic pixels (Table 2). The model achieves strong performance with RMSE of 11.2 Myr and minimal mean bias of −1.5 Myr (−2.5%), indicating negligible systematic offset. The model exhibits very strong linear correlation (Pearson $r = 0.97$, $R^2 = 0.94$) and excellent predictive skill (Index of Agreement = 0.98), substantially exceeding the performance of a mean-age baseline. Half of all pixels show absolute errors below 2.4 Myr, with 90% below 12.6 Myr and 95% below 19.9 Myr, demonstrating robust agreement across the global ocean basins. The Wasserstein

Table 1: Validation statistics for present-day palaeogeography against ETOPO 2022 at 10 km resolution. Statistics are reported for global, continental (COB-defined landmasses), and oceanic domains separately.

Metric	**Global**	**Continental**	**Oceanic**
Number of pixels	5,092,897	2,032,190	3,060,707
Error metrics (Model vs. ETOPO 2022)			
RMSE (m)	950	1057	871
Mean bias (m)	−25.1	−38.1	−16.5
Mean absolute error (m)	620	670	587
Median absolute error (m)	375	355	386
Correlation and skill scores			
Pearson r	0.920	0.536	0.626
Spearman ρ	0.887	0.454	0.695
R^2	0.845	0.196	0.370
Index of Agreement	0.958	0.707	0.773
Distribution comparison			
Wasserstein distance (m)	177	190	203
K-S statistic	0.096^{***}	0.179^{***}	0.159^{***}

$^{***}p < 0.001$ (distributions significantly different)

distance of 1.9 Myr reflects minimal distributional offset relative to the 299.8 Myr range in observed ages. Nearly identical Pearson ($r = 0.9706$) and Spearman ($\rho = 0.9726$) correlations confirm an approximately linear relationship throughout the age range.

The small Kolmogorov-Smirnov statistic (0.04) indicates minor distributional differences despite high correlation, likely reflecting subtle differences in isochron interpretation or interpolation methodology between the two models rather than fundamental disagreement on crustal ages. The low median absolute error (2.4 Myr) demonstrates that the vast majority of the ocean floor is accurately dated by the plate reconstruction. Larger errors (99th percentile: 49.5 Myr, maximum: 167.9 Myr) are concentrated in regions with complex tectonic histories, including back-arc basins, microplate boundaries, and areas affected by ridge jumps or diffuse deformation, where magnetic lineations are ambiguous and age assignments inherently uncertain in both models.

These results demonstrate that the PANALESIS plate reconstruction successfully reproduces the global pattern of seafloor ages, validating the kinematic framework and isochron identifications that underpin the model. The high skill score (IoA = 0.98) confirms that seafloor age, as the most directly observable constraint on plate motions, is accurately predicted by the reconstruction and provides a reliable foundation for deriving secondary variables such as bathymetry and oceanic crustal thickness.

4.5 Crustal Thickness

Present-day crustal thickness from the PANALESIS Atlas is validated against CRUST 2.0[35] at 200 km resolution across 12,800 valid pixels (Table 3). Globally, the model achieves an RMSE of 5.6 km with negligible mean bias of −0.1 km (−0.8%), indicating near-unbiased prediction of mean crustal thickness.

Table 2: Validation statistics for present-day seafloor age against the global seafloor age grid of Seton et al.[59] at 10 km resolution. Analysis includes oceanic regions only as defined by the COB.

Metric	**Oceanic**
Number of pixels	2,879,872
Error metrics (Model vs. Seton et al. 2020)	
RMSE (Myr)	11.2
Mean bias (Myr)	−1.5
Mean absolute error (Myr)	5.4
Median absolute error (Myr)	2.4
Correlation and skill scores	
Pearson r	0.971
Spearman ρ	0.973
R^2	0.941
Index of Agreement	0.985
Distribution comparison	
Wasserstein distance (Myr)	1.9
K-S statistic	0.037^{***}

$^{***}p < 0.001$ (distributions significantly different)

The model exhibits strong linear correlation (Pearson $r = 0.92$, $R^2 = 0.84$) and high predictive skill (Index of Agreement = 0.96), demonstrating robust agreement with seismically derived crustal structure. Half of all pixels show absolute errors below 0.9 km, with 90% below 9.7 km. The Wasserstein distance of 1.9 km indicates only modest distributional offset relative to the observed global thickness range of 67.2 km.

Regional performance varies systematically by tectonic domain. In continental regions (5,153 pixels), the model shows moderate correlation ($r = 0.61$, $R^2 = 0.28$) with an RMSE of 7.7 km and a positive mean bias of +1.8 km (+5.3%), reflecting a tendency to overestimate continental crustal thickness. The discrepancy between Pearson ($r = 0.61$) and Spearman ($\rho = 0.51$) correlations suggests non-monotonic errors, likely arising from difficulties in reproducing localised crustal thickening and thinning associated with orogenesis and continental extension using plate kinematic constraints alone.

In oceanic regions (7,647 pixels), the model attains lower overall skill, with an RMSE of 3.6 km and a systematic negative bias of −1.4 km (−17.3%). Correlation remains moderate ($r = 0.57$, $\rho = 0.50$), indicating that first-order spatial patterns in oceanic crustal thickness are captured. However high Kolmogorov-Smirnov statistic (0.32) reflects the model's tendency to predict uniform normal oceanic crust thickness (∼6.5 km), failing to reproduce the thickened crust observed in oceanic plateaus, ridges, and large igneous provinces included in CRUST 2.0. Median absolute errors are markedly lower in oceanic domains (0.0 km) than in continental domains (3.9 km), though extreme errors persist in both settings (99th percentile: 15.0 km oceanic; 23.6 km continental).

Overall, these results demonstrate that plate tectonic reconstruction combined with a power-law elevation-thickness relationship successfully reproduces global mean crustal structure and large-scale

continental thickness patterns. However, capturing the full variability of crustal thickness, particularly in oceanic regions, remains challenging without explicit representation of hotspot volcanism, plume-ridge interactions, and crustal modification processes beyond seafloor spreading.

Table 3: Validation statistics for present-day crustal thickness against CRUST 2.0 at 200 km resolution. Statistics are reported for global, continental (COB-defined landmasses), and oceanic domains separately.

Metric	**Global**	**Continental**	**Oceanic**
Number of pixels	12,800	5,153	7,647
Error metrics (Model vs. CRUST 2.0)			
RMSE (km)	5.6	7.7	3.6
Mean bias (km)	−0.1	+1.8	−1.4
Mean absolute error (km)	3.1	5.6	1.5
Median absolute error (km)	0.9	3.9	0.0
Correlation and skill scores			
Pearson r	0.924	0.605	0.574
Spearman ρ	0.889	0.512	0.501
R^2	0.836	0.284	0.166
Index of Agreement	0.960	0.762	0.593
Distribution comparison			
Wasserstein distance (km)	1.9	3.0	1.4
K-S statistic	0.193^{***}	0.255^{***}	0.321^{***}

$^{***}p < 0.001$ (distributions significantly different)

4.6 Lithospheric Thickness

Present-day lithospheric thickness from the PANALESIS Atlas is validated against LithoRef18[63] at 200 km resolution across 12,800 valid pixels (Table 4). Globally, the model achieves an RMSE of 32.7 km with negligible mean bias of +0.5 km (+0.5%), indicating accurate reproduction of mean lithospheric structure. The model exhibits moderate correlation (Pearson $r = 0.64$, $R^2 = 0.21$) and modest predictive skill (Index of Agreement = 0.79), indicating the model captures broad-scale patterns but substantial local variance remains unexplained. Half of all pixels show absolute errors below 16.4 km, with 90% below 55.3 km. The Wasserstein distance of 5.3 km reflects small distributional offset relative to the 191.8 km range in observed thicknesses.

Regional performance diverges strongly by tectonic domain. In continental regions (5,153 pixels), the model shows weak correlation ($r = 0.45$, $R^2 = 0.09$) with RMSE of 44.7 km and minimal bias of −0.2 km. Continental lithospheric thickness is controlled by complex thermal and compositional evolution over billions of years, including cratonic stabilisation, lithospheric delamination, metasomatism, and variable heat flow-processes not captured by present-day plate boundaries and ages. The difference between Pearson ($r = 0.45$) and Spearman ($\rho = 0.38$) correlations suggests non-monotonic errors. The large K-S statistic (0.23) and Wasserstein distance (17.5 km) indicate distributional mismatch, particularly in capturing the full range of thick cratonic lithosphere.

In contrast, oceanic regions (7,647 pixels) show strong performance with high correlation ($r = 0.89$, $\rho = 0.90$) despite modest skill score (RMSE = 21.1 km). The strong correlation but low R^2 (0.26) reflects systematic scaling differences: the model captures the monotonic relationship between seafloor age and lithospheric thickness (thermal boundary layer growth) but with different thermal parameters or reference depths than LithoRef18. Median absolute errors are markedly lower in oceanic (12.5 km) than continental (33.3 km) domains, and extreme errors (99th percentile: 60.4 km oceanic vs. 114.9 km continental) are also smaller, consistent with more predictable thermal evolution in oceanic settings. The oceanic K-S statistic (0.24) indicates distributional differences likely stemming from variations in assumed thermal structure or lithosphere-asthenosphere boundary definitions between models.

These results demonstrate that plate tectonic models successfully predict oceanic lithospheric thermal structure from seafloor age but struggle to capture continental lithospheric thickness variations, which are controlled by protracted tectonic inheritance rather than present-day plate configuration. The strong oceanic correlations validate the thermal cooling framework, while continental limitations highlight the need for explicit treatment of deep lithospheric composition and ancient thermal events.

Table 4: Validation statistics for present-day lithospheric thickness against LithoRef18 at 200 km resolution. Statistics are reported for global, continental (COB-defined landmasses), and oceanic domains separately.

Metric	**Global**	**Continental**	**Oceanic**
Number of pixels	12,800	5,153	7,647
Error metrics (Model vs. LithoRef18)			
RMSE (km)	32.7	44.7	21.1
Mean bias (km)	+0.5	−0.2	+1.1
Mean absolute error (km)	24.3	36.4	16.1
Median absolute error (km)	16.4	33.3	12.5
Correlation and skill scores			
Pearson r	0.635	0.449	0.885
Spearman ρ	0.644	0.381	0.904
R^2	0.212	0.093	0.257
Index of Agreement	0.791	0.664	0.886
Distribution comparison			
Wasserstein distance (km)	5.3	17.5	13.5
K-S statistic	0.078^{***}	0.228^{***}	0.239^{***}

$^{***}p < 0.001$ (distributions significantly different)

4.7 Climate

Present-day outputs generated with the PLASIM-GENIE model and based on the PANALESIS-derived palaeogeography were compared to the PLASIM-GENIE reference outputs for present-day by Holden et al.[30]. Before comparing, original grids following the PLASIM-GENIE resolutions were resampled to an equal area grid of 500 by 500km by extracting original pixel centroids and interpolating them into the

new grid. For precipitation, units were also converted from m/s to mm/year.

4.7.1 Surface Air Temperature

Present-day surface temperature from the PANALESIS Atlas is validated against Holden et al.[30] across 2,080 valid pixels (Table 5). Globally, the model achieves an RMSE of 12.0 °C with a small mean bias of +1.0 °C (+5.9%), indicating broadly accurate reproduction of mean temperature structure. The model shows moderate-to-good correlation (Pearson $r = 0.75$, Spearman $\rho = 0.87$, $R^2 = 0.33$) and meaningful predictive skill (Index of Agreement = 0.85), indicating the model captures broad-scale spatial patterns while leaving substantial local variance unexplained. Half of all pixels show absolute errors below 4.2 °C, with 90% below 18.7 °C. The Wasserstein distance of 3.3 °C reflects a small distributional offset relative to the 77.2 °C observed range. The consistently higher Spearman than Pearson correlation ($\Delta = +0.12$) suggests the model captures monotonic temperature gradients but with some non-linear scaling relative to the reference.

Regional performance diverges by tectonic domain. In continental regions (843 pixels), the model shows moderate correlation ($r = 0.66$, $\rho = 0.77$, $R^2 = 0.12$) with RMSE of 18.0 °C and small mean bias of −1.1 °C. Continental temperatures are governed by complex interactions between elevation, continental geometry, proximity to moisture sources, and long-term climate feedbacks tied to paleogeographic boundary conditions-processes only partially constrained by plate kinematic models. The pronounced difference between Pearson ($r = 0.66$) and Spearman ($\rho = 0.77$) correlations suggests non-linear errors, and the moderate K-S statistic (0.11) with Wasserstein distance of 3.8 °C indicates partial distributional mismatch, particularly in reproducing the full range of continental temperature extremes.

In stark contrast, oceanic regions (1,237 pixels) show strong performance with high correlation ($r = 0.93$, $\rho = 0.95$) and high predictive skill (RMSE = 4.8 °C, $R^2 = 0.75$). The close agreement between Pearson and Spearman correlations indicates an approximately linear model- -reference relationship in oceanic settings, consistent with well-constrained sea-surface temperature gradients tied to basin geometry and oceanic circulation patterns. Median absolute errors are markedly lower over oceans (3.1 °C) than continents (9.5 °C), and extreme errors (99th percentile: 17.6 °C oceanic vs. 54.6 °C continental) are substantially smaller, reflecting more predictable thermal boundary conditions in open-ocean settings. The oceanic K-S statistic (0.24) indicates residual distributional differences, likely stemming from model limitations in capturing polar and upwelling regions at the tails of the sea-surface temperature distribution.

These results demonstrate that the plate tectonic framework successfully reproduces large-scale oceanic temperature patterns but is less skilful over continents, where surface temperature is governed by a broader array of paleogeographic, orographic, and atmospheric feedbacks. The strong oceanic skill scores validate the thermal boundary conditions employed, while continental limitations highlight

the need for improved treatment of land surface processes and atmospheric dynamics in future model iterations.

Table 5: Validation statistics for present-day surface temperature against Holden et al.[30]. Statistics are reported for global, continental (COB-defined landmasses), and oceanic domains separately.

Metric	**Global**	**Continental**	**Oceanic**
Number of pixels	2,080	843	1,237
Error metrics (Model vs. Holden et al. 2016)			
RMSE (°C)	12.0	18.0	4.8
Mean bias (°C)	+1.0	−1.1	+2.5
Mean absolute error (°C)	7.6	13.1	3.8
Median absolute error (°C)	4.2	9.5	3.1
Correlation and skill scores			
Pearson r	0.750	0.661	0.932
Spearman ρ	0.867	0.765	0.948
R^2	0.333	0.119	0.747
Index of Agreement	0.850	0.800	0.945
Distribution comparison			
Wasserstein distance (°C)	3.3	3.8	3.3
K-S statistic	0.183^{***}	0.110^{***}	0.239^{***}

$^{***}p < 0.001$ (distributions significantly different)

4.7.2 Precipitation

Present-day precipitation from the PANALESIS Atlas is validated against Holden et al.[30] across 2,080 valid pixels (Table 6). Globally, the model achieves an RMSE of 730.4 mm yr^{-1} with a modest mean bias of +70.5 mm yr^{-1} (+7.7%), indicating limited overall skill despite reasonable reproduction of the mean. Correlation is moderate (Pearson $r = 0.58$, Spearman $\rho = 0.59$, $R^2 = -0.37$), with the negative R^2 indicating the model performs worse than a simple mean-value baseline in terms of explained variance, a consequence of high dispersion in errors relative to the observed spread. The Index of Agreement (0.74) nevertheless reflects partial correspondence in spatial patterns. Half of all pixels show absolute errors below 303.9 mm yr^{-1}, with 90% below 1122.3 mm yr^{-1}. The Wasserstein distance of 136.5 mm yr^{-1} and the significantly different distributions (K-S = 0.07, $p < 0.001$) indicate the model overestimates the spread and upper tail of the precipitation distribution, consistent with the model's substantially larger standard deviation (882.6 vs. 624.3 mm yr^{-1}) and high kurtosis.

Regional performance is poor in both domains, though for different reasons. In continental regions (843 pixels), the model shows weak correlation ($r = 0.47$, $\rho = 0.49$, $R^2 = -0.66$) with RMSE of 937.6 mm yr^{-1} and a mean bias of +88.6 mm yr^{-1} (+10.8%). Continental precipitation is governed by orographic forcing, large-scale atmospheric circulation, monsoon dynamics, and the positions of moisture sources-processes that depend critically on continental geometry, topography, and seasonal insolation gradients that are only coarsely approximated in a plate kinematic framework. The K-S statistic (0.05)

is not significant ($p = 0.18$), suggesting that while pixel-level errors are large, the continental precipitation distribution is broadly reproduced in aggregate. The extreme error range (-3118.7 to $+7396.5$ mm yr^{-1}) points to localised failures in high-precipitation regions such as tropical convergence zones and orographic belts.

Oceanic regions (1,237 pixels) show improved but still limited performance, with higher correlation ($r = 0.71$, $\rho = 0.69$) than the continental domain but negative skill score (RMSE = 545.9 mm yr^{-1}). Median absolute errors are modestly lower over oceans (289.8 mm yr^{-1}) than continents (337.6 mm yr^{-1}), and the larger Wasserstein distance over oceans (161.7 vs. 109.5 mm yr^{-1}) reflects the greater distributional mismatch introduced by these extreme values.

These results demonstrate that the plate tectonic framework struggles to reproduce precipitation patterns at the pixel scale in both continental and oceanic domains, with errors dominated by variance inflation and localised extremes rather than systematic mean bias. The moderate spatial correlations ($r \approx$ 0.47-0.71) indicate the model captures first-order zonal precipitation gradients. Improved precipitation skill will likely require coupling to an atmospheric circulation model or the incorporation of paleoaltimetry constraints.

Table 6: Validation statistics for present-day precipitation against Holden et al.[30]. Statistics are reported for global, continental (COB-defined landmasses), and oceanic domains separately.

Metric	**Global**	**Continental**	**Oceanic**
Number of pixels	2,080	843	1,237
Error metrics (Model vs. Holden et al. 2016)			
RMSE (mm yr^{-1})	730.4	937.6	545.9
Mean bias (mm yr^{-1})	+70.5	+88.6	+58.2
Mean absolute error (mm yr^{-1})	467.0	589.4	383.6
Median absolute error (mm yr^{-1})	303.9	337.6	289.8
Correlation and skill scores			
Pearson r	0.581	0.470	0.710
Spearman ρ	0.585	0.485	0.685
R^2	-0.369	-0.662	-0.051
Index of Agreement	0.736	0.667	0.808
Distribution comparison			
Wasserstein distance (mm yr^{-1})	136.5	109.5	161.7
K-S statistic	0.065^{***}	$0.053^{\dagger}$	0.091^{***}

$^{***}p < 0.001$; $^{\dagger}p = 0.18$ (distributions not significantly different)

4.8 Cross-Variable Synthesis and Limitations

First, for all variables, error metrics might appear large, especially when looking at absolute values. Yet, it is to be acknowledged that our maps are all generated from a single, standalone model describing plate tectonics, which is a representation of the world that only considers plate positions and movement at the global scale, with its own uncertainties and spatial scale to represent geodynamic settings[25].

Second, considering that all products still show good to excellent metrics globally is an indication that error propagation remains limited and our approximations are realistic, allowing, ad minimum, to do a first-order estimate of the various aspect depicted by our products. For instance, the performance of the lithospheric thickness map may be considered poor when looking at performance metrics such as the RMSE of 33.4 km (compared to LithoRef18[63]). However, many models based on present-day observations have much higher errors. For instance, Tenzer & Chen[71] have reported that models have a mean RMSE of about ±40 km,with some very high error values, like LITHO1[60] versus SLNAAFSA 77km, versus SL2013sv 74km, CAM2016 71, and 3d2015-075V 74km, which is partially represented in Fig. 9.

Finally, the dataset we provide in this study is not focused on the present-day alone, but extends these global maps to the entire Phanerozoic, with 45 time steps, allowing deep-time understanding of the Earth system evolution through deep-time using only one consistent source of data.

Fig. 9 presents kernel density estimates (KDE) comparing the full pixel-level distributions of PANALESIS products against reference datasets at their respective validation resolutions. The distributional agreement reinforces the quantitative metrics reported above. Palaeogeography shows overall agreement between the ETOPO 2022 and PANALESIS bimodal distribution with minor peaks overestimation due to synthetic nature of the reconstructed topography. Seafloor age exhibits near-perfect distributional matching, consistent with the lowest RMSE and highest R^2 values among all variables. Crustal thickness accurately reproduces the characteristic bimodal distribution (oceanic 7 km, continental 35 km) with minimal offset. Lithospheric thickness (Fig. 9d) captures the broad structure of the reference distribution, though with slightly reduced variance in continental regions, reflecting the greater uncertainty inherent in both model and observations for this variable.

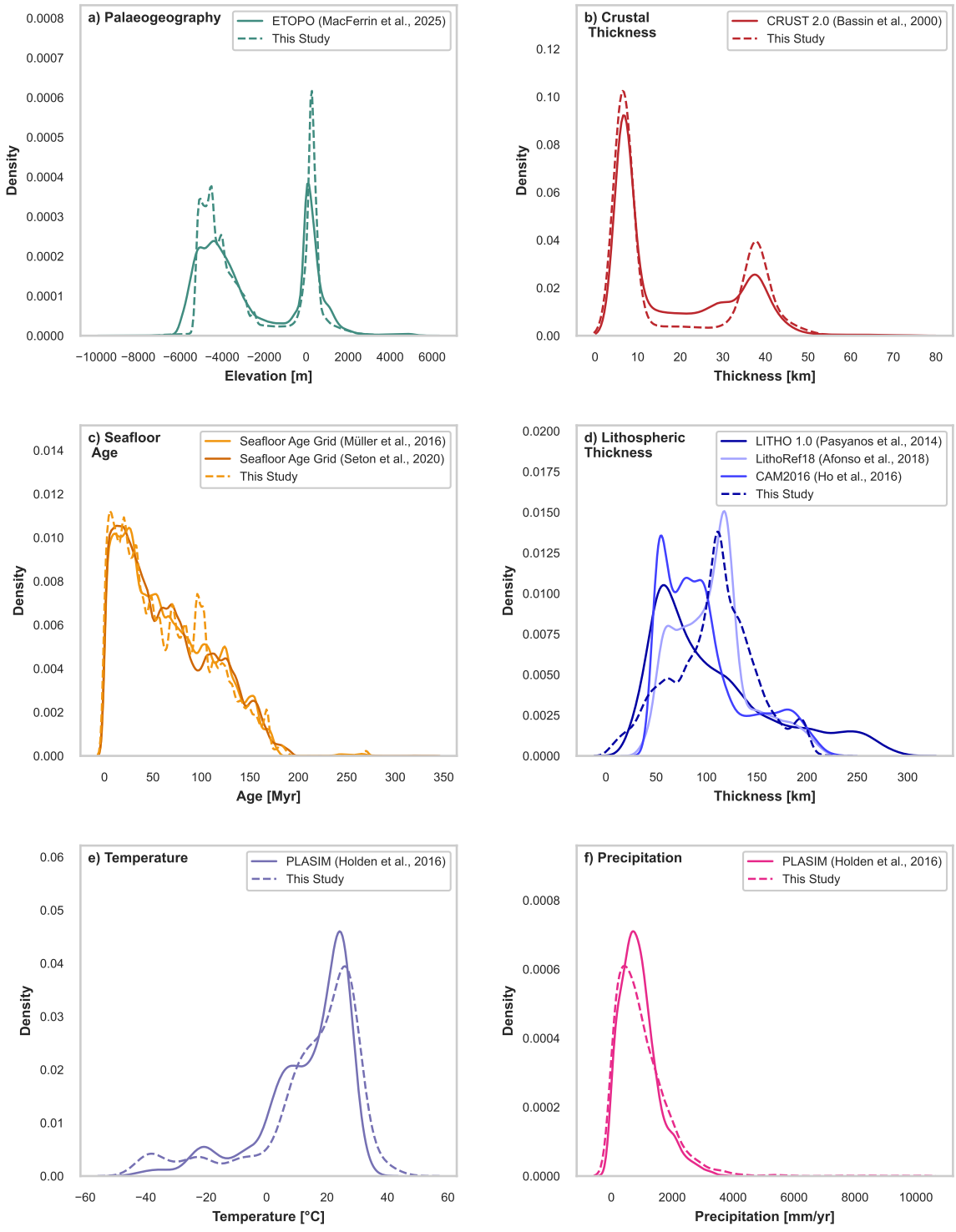

Figure 9: Kernel density estimate plots comparing PANALESIS Atlas products (dashed lines) with reference datasets (solid lines) for present-day validation. (a) Palaeogeography validated against ETOPO 2022 at 10 km resolution. (b) Seafloor age validated against the Seton et al. (2020) global age grid at 10 km resolution. (c) Crustal thickness validated against CRUST 2.0 at 200 km resolution. (d) Lithospheric thickness validated against LITHO 1.0, CAM2016 and LithoRef18 at 200 km resolution. (e) Surface air temperature validated against PLASIM reference outputs from Holden et al. (2016). (f) Precipitation validated against PLASIM reference outputs from Holden et al. (2016). All comparisons use identical spatial extents and continent-ocean masks.

5 Usage Notes

The layers of this dataset may be used for different aspects of deep-time Earth system modelling. First, the palaeogeographic maps are useful for constraining boundary conditions of climate models, biogeographic simulations needing temporally coherent land-sea masks, or assessing sea-level variations throughout the Phanerozoic [29].

Furthermore, combining palaeogeography with precipitation and temperature allows to model Earth surface dynamic processes such as hydrological modelling, with flow paths tracing, flow length calculations, drainage basins delineation, and sediment fluxes estimation. Other layers, such as crustal or lithospheric thickness may be used in geodynamic modelling to constrain surface parameters, or to understand the interaction between the oceanic crust and seawater at mid-oceanic ridges. All layers are available in GeoTIFF format, with accompanying code and metadata to support reproducibility and integration into GIS workflows or Earth system models.

6 Data Availability

All datasets generated for the PANALESIS Atlas are publicly available under the DOI: https://doi.org/10.5281/zenodo.19134591. The unified release, titled *"A Phanerozoic Atlas of Earth's Atmosphere, Surface, and Interior Derived from the PANALESIS Plate Tectonic Model"*, includes maps described in this manuscript, in their original cylindrical equal area projection (ESRI:54034) named "EqualArea" in the data record, and in decimal degrees (EPSG:4326), named "LatLong" in the data record.

Moreover, the data is accessible through the *Palaeo Data Cube* platform, at the following URL: https://github.com/florianfranz/palaeo-data-cube. he Palaeo Data Cube (PDC) provides global maps of the Earth in deep-time (currently of the last 545 million years, in 45 steps). It is inspired by the present-day Earth Observations (EO) Data Cubes, and provides access to data products in high-resolution of the Earth system long-term evolution.

7 Code Availability

All source code used to generate the datasets and figures in this study is openly available under permissive licenses:

- The PANALESIS Atlas workflow, is hosted on GitHub: https://github.com/florianfranz/panalesis_atlas.
- The palaeogeographic reconstruction plugin for QGIS (TopoChronia), which underpins the atlas by producing palaeogeographic maps, is available at: https://github.com/florianfranz/topo_chronia [29].

Both repositories include detailed documentation, example workflows, and environment specifications to ensure reproducibility. The code is distributed under open-source licenses (GPL-2.0 for TopoChronia, MIT for PANALESIS Atlas).

8 Acknowledgments

The authors acknowledge funding from the Swiss National Science Foundation (SNSF) grant #213539: *Long-term evolution of the Earth from the base of the mantle to the top of the atmosphere: Understanding the mechanisms leading to 'greenhouse' and 'icehouse' regimes*

9 Competing Interests

The authors declare having no competing financial interests. Grégory Giuliani is currently an Editorial Board member for Scientific Data.

References

[1] Barron, E. J., Thompson, S. L. & Hay, W. W. Continental distribution as a forcing factor for global-scale temperature. *Nature* **310**, 574–575 (1984).

[2] Donnadieu, Y., Goddéris, Y., Ramstein, G., Nédélec, A. & Meert, J. A 'snowball Earth' climate triggered by continental break-up through changes in runoff. *Nature* **428**, 303–306 (2004).

[3] Donnadieu, Y., Pucéat, E., Moiroud, M., Guillocheau, F. & Deconinck, J.-F. A better-ventilated ocean triggered by Late Cretaceous changes in continental configuration. *Nature Communications* **7**, 10316 (2016).

[4] Niezgodzki, I., Tyszka, J., Knorr, G. & Lohmann, G. Was the Arctic Ocean ice free during the latest Cretaceous? The role of CO2 and gateway configurations. *Global and Planetary Change* **177**, 201–212 (2019).

[5] Barker, P. F. Scotia Sea regional tectonic evolution: Implications for mantle flow and palaeocirculation. *Earth-Science Reviews* **55**, 1–39 (2001).

[6] Verard, C. & Veizer, J. On plate tectonics and ocean temperatures. *Geology* **47**, 881 (2019).

[7] Servais, T. & Harper, D. A. The Great Ordovician Biodiversification Event (GOBE): Definition, concept and duration. *Lethaia* **51**, 151–164 (2018).

[8] Vérard, C. Plate tectonic modelling: Review and perspectives. *Geological Magazine* **156**, 208–241 (2019).

[9] Merdith, A. S. *et al.* Extending full-plate tectonic models into deep time: Linking the Neoproterozoic and the Phanerozoic. *Earth-Science Reviews* **214**, 103477 (2021).

[10] Scotese, C. An Atlas of Phanerozoic Paleogeographic Maps: The Seas Come In and the Seas Go Out. *Annual Review of Earth and Planetary Sciences* **49**, 679–728 (2021).

[11] Cawood, P. A. *et al.* Secular Evolution of Continents and the Earth System. *Reviews of Geophysics* **60**, e2022RG000789 (2022).

[12] Seton, M., Williams, S. E., Domeier, M., Collins, A. S. & Sigloch, K. Deconstructing plate tectonic reconstructions. *Nature Reviews Earth & Environment* **4**, 185–204 (2023).

[13] Cao, X. *et al.* Earth's tectonic and plate boundary evolution over 1.8 billion years. *Geoscience Frontiers* **15**, 101922 (2024).

[14] Miller, K. G. *et al.* The Phanerozoic Record of Global Sea-Level Change. *Science* **310**, 1293–1298 (2005).

[15] Vérard, C., Hochard, C., Baumgartner, P. O., Stampfli, G. M. & Liu, M. 3D palaeogeographic reconstructions of the Phanerozoic versus sea-level and Sr-ratio variations. *Journal of Palaeogeography* **4**, 64–84 (2015).

[16] Marcilly, C. M., Torsvik, T. H. & Conrad, C. P. Global Phanerozoic sea levels from paleogeographic flooding maps. *Gondwana Research* **110**, 128–142 (2022).

[17] Franziskakis, F., Vérard, C., Castelltort, S. & Giuliani, G. Comparing 545 Million Years of Sea-Level Change: New Insights from the TopoChronia QGIS Plugin. *The International Archives of the Photogrammetry, Remote Sensing and Spatial Information Sciences* **XLVIII-4-W13-2025**, 111–118 (2025).

[18] Goddéris, Y., Donnadieu, Y., Le Hir, G., Lefebvre, V. & Nardin, E. The role of palaeogeography in the Phanerozoic history of atmospheric CO2 and climate. *Earth-Science Reviews* **128**, 122–138 (2014).

[19] Scotese, C. R., Song, H., Mills, B. J. W. & van der Meer, D. G. Phanerozoic paleotemperatures: The earth's changing climate during the last 540 million years. *Earth-Science Reviews* **215**, 103503 (2021).

[20] Valentine, J. W. & Moores, E. M. Plate Tectonics and the History of Life in the Oceans. *Scientific American* **230**, 80–89 (1974). 24950054.

[21] Stern, R. J. Is plate tectonics needed to evolve technological species on exoplanets? *Geoscience Frontiers* **7**, 573–580 (2016).

[22] Stern, R. J. & Gerya, T. V. The importance of continents, oceans and plate tectonics for the evolution of complex life: Implications for finding extraterrestrial civilizations. *Scientific Reports* **14**, 8552 (2024).

[23] Westall, F. & Xiao, S. Precambrian Earth: Co-evolution of life and geodynamics. *Precambrian Research* **414**, 107589 (2024).

[24] Markwick, P. J. Palaeogeography in exploration. *Geological Magazine* **156**, 366–407 (2019).

[25] Vérard, C. Panalesis: Towards global synthetic palaeogeographies using integration and coupling of manifold models. *Geological Magazine* **156**, 320–330 (2019).

[26] Vérard, C., Hochard, C., Baumgartner, P. O., Stampfli, G. M. & Liu, M. Geodynamic evolution of the Earth over the Phanerozoic: Plate tectonic activity and palaeoclimatic indicators. *Journal of Palaeogeography* **4**, 167–188 (2015).

[27] Lyster, S. J., Whittaker, A. C., Allison, P. A., Lunt, D. J. & Farnsworth, A. Predicting sediment discharges and erosion rates in deep time—examples from the late Cretaceous North American continent. *Basin Research* **32**, 1547–1573 (2020).

[28] Müller, R. D., Sdrolias, M., Gaina, C. & Roest, W. R. Age, spreading rates, and spreading asymmetry of the world's ocean crust. *Geochemistry, Geophysics, Geosystems* **9** (2008).

[29] Franziskakis, F., Vérard, C., Castelltort, S. & Giuliani, G. TopoChronia: A QGIS plugin for the creation of fully quantified palaeogeographic maps. *Journal of Open Source Software* **11**, 8812 (2026).

[30] Holden, P. B. *et al.* PLASIM–GENIE v1.0: A new intermediate complexity AOGCM. *Geoscientific Model Development* **9**, 3347–3361 (2016).

[31] Vérard, C. 888–444 Ma Global Plate Tectonic Reconstruction With Emphasis on the Formation of Gondwana. *Frontiers in Earth Science* **9** (2021).

[32] Virtanen, P. *et al.* SciPy 1.0: Fundamental algorithms for scientific computing in Python. *Nature Methods* **17**, 261–272 (2020).

[33] Barber, C. B., Dobkin, D. P. & Huhdanpaa, H. The quickhull algorithm for convex hulls. *ACM Trans. Math. Softw.* **22**, 469–483 (1996).

[34] Rouault, E. *et al.* GDAL. Zenodo (2025).

[35] Bassin, C. The Current Limits of resolution for surface wave tomography in North America. *Eos, Transactions American Geophysical Union* (2000).

[36] Cawood, P. A. & Hawkesworth, C. J. Continental crustal volume, thickness and area, and their geodynamic implications. *Gondwana Research* **66**, 116–125 (2019).

[37] Vérard, C. Statistics of the Earth's Topography. *OALib* **04**, 1–50 (2017).

[38] Priestley, K., Ho, T. & Mitra, S. The crustal structure of the Himalaya: A synthesis. *Geological Society, London, Special Publications* **483**, 483–516 (2019).

[39] Hazarika, D., Kumar, N. & Yadav, D. K. Crustal thickness and Poisson's ratio variations across the northwest Himalaya and eastern Ladakh. *Acta Geophysica* **61**, 905–922 (2013).

[40] Parsons, B. & Sclater, J. G. An analysis of the variation of ocean floor bathymetry and heat flow with age. *Journal of Geophysical Research (1896-1977)* **82**, 803–827 (1977).

[41] Stein, C. A. & Stein, S. A model for the global variation in oceanic depth and heat flow with lithospheric age. *Nature* **359**, 123–129 (1992).

[42] Turcotte, D. L. & Schubert, G. *Geodynamics* (Cambridge University Press, Cambridge, 2002), 2 edn.

[43] Rychert, C. A., Harmon, N., Constable, S. & Wang, S. The Nature of the Lithosphere-Asthenosphere Boundary. *Journal of Geophysical Research: Solid Earth* **125**, e2018JB016463 (2020).

[44] Fischer, K. M. *et al.* A comparison of oceanic and continental mantle lithosphere. *Physics of the Earth and Planetary Interiors* **309**, 106600 (2020).

[45] Dalton, C. A., Bao, X. & Ma, Z. The thermal structure of cratonic lithosphere from global Rayleigh wave attenuation. *Earth and Planetary Science Letters* **457**, 250–262 (2017).

[46] Artemieva, I. M. & Mooney, W. D. Thermal thickness and evolution of Precambrian lithosphere: A global study. *Journal of Geophysical Research: Solid Earth* **106**, 16387–16414 (2001).

[47] Gernon, T. M. *et al.* Coevolution of craton margins and interiors during continental break-up. *Nature* **632**, 327–335 (2024).

[48] Spohn, T. & Schubert, G. Convective thinning of the lithosphere: A mechanism for the initiation of continental rifting. *Journal of Geophysical Research: Solid Earth* **87**, 4669–4681 (1982).

[49] Gibson, S. A. *et al.* Asthenosphere-derived magmatism in the Rio Grande rift, western USA: Implications for continental break-up. *Geological Society, London, Special Publications* **68**, 61–89 (1992).

[50] Zorin, Y. A., Kozhevnikov, V. M., Novoselova, M. R. & Turutanov, E. K. Thickness of the lithosphere beneath the Baikal rift zone and adjacent regions. *Tectonophysics* **168**, 327–337 (1989).

[51] Rychert, C. A. & Shearer, P. M. A Global View of the Lithosphere-Asthenosphere Boundary. *Science* **324**, 495–498 (2009).

[52] Fraedrich, K., Jansen, H., Kirk, E., Luksch, U. & Lunkeit, F. The Planet Simulator: Towards a user friendly model. *Meteorologische Zeitschrift* **14**, 299–304 (2005).

[53] Lenton, T. M., Daines, S. J. & Mills, B. J. W. COPSE reloaded: An improved model of biogeochemical cycling over Phanerozoic time. *Earth-Science Reviews* **178**, 1–28 (2018).

[54] Gough, D. O. Solar interior structure and luminosity variations. *Solar Physics* **74**, 21–34 (1981).

[55] Le Hir, G. *et al.* The climate change caused by the land plant invasion in the Devonian. *Earth and Planetary Science Letters* **310**, 203–212 (2011).

[56] Pohl, A., Wong Hearing, T., Franc, A., Sepulchre, P. & Scotese, C. R. Dataset of Phanerozoic continental climate and Köppen–Geiger climate classes. *Data in Brief* **43**, 108424 (2022).

[57] MacFerrin, M., Amante, C., Carignan, K., Love, M. & Lim, E. The Earth Topography 2022 (ETOPO 2022) global DEM dataset. *Earth System Science Data* **17**, 1835–1849 (2025).

[58] Müller, R. D. *et al.* Ocean Basin Evolution and Global-Scale Plate Reorganization Events Since Pangea Breakup. *Annual Review of Earth and Planetary Sciences* **44**, 107–138 (2016).

[59] Seton, M. *et al.* A Global Data Set of Present-Day Oceanic Crustal Age and Seafloor Spreading Parameters. *Geochemistry, Geophysics, Geosystems* **21**, e2020GC009214 (2020).

[60] Pasyanos, M. E., Masters, T. G., Laske, G. & Ma, Z. LITHO1.0: An updated crust and lithospheric model of the Earth. *Journal of Geophysical Research: Solid Earth* **119**, 2153–2173 (2014).

[61] Ho, T., Priestley, K. & Debayle, E. A global horizontal shear velocity model of the upper mantle from multimode Love wave measurements. *Geophysical Journal International* **207**, 542–561 (2016).

[62] Trabant, C. *et al.* Data Products at the IRIS DMC: Stepping Stones for Research and Other Applications. *Seismological Research Letters* **83**, 846–854 (2012).

[63] Afonso, J. C., Salajegheh, F., Szwillus, W., Ebbing, J. & Gaina, C. A global reference model of the lithosphere and upper mantle from joint inversion and analysis of multiple data sets. *Geophysical Journal International* **217**, 1602–1628 (2019).

[64] Villani, C. *Topics in Optimal Transportation* (American Mathematical Soc., 2003).

[65] Peyré, G. & Cuturi, M. Computational Optimal Transport: With Applications to Data Science. *Foundations and Trends® in Machine Learning* **11**, 355–607 (2019).

[66] Lipp, A. & Vermeesch, P. Short communication: The Wasserstein distance as a dissimilarity metric for comparing detrital age spectra and other geological distributions. *Geochronology* **5**, 263–270 (2023).

[67] Willmott, C. J. On the Validation of Models. *Physical Geography* **2**, 184–194 (1981).

[68] Kolmogorov, A. Sulla determinazione empirica di una legge didistribuzione. *Giorn Dell'inst Ital Degli Att* **4**, 89–91 (1933).

[69] Smirnov, N. Table for Estimating the Goodness of Fit of Empirical Distributions. *The Annals of Mathematical Statistics* **19**, 279–281 (1948).

[70] Spearman, C. The Proof and Measurement of Association between Two Things. *The American Journal of Psychology* **15**, 72–101 (1904). 1412159.

[71] Tenzer, R. & Chen, W. The Accuracy Assessment of Lithospheric Density Models. *Applied Sciences* **13**, 10432 (2023).